PAPER

Check for updates

Organoceria nanostructured hybrid materials: a novel approach for band gap modulation in ceria

María Puerto-Jiménez, [a] Enqi Bu, [a,b] Daniel Goma, [c,d] Almudena Aguinaco, [b,e] Juan José Delgado, [a,b] José María Pintado, [a,b] Ginesa Blanco [a,b] and Adrián Bogeat Barroso *[f]

The development of efficient visible light photocatalysts based on ceria (CeO_2) requires precise control over both morphology and electronic band structure. Herein, a facile one-pot hydrothermal method is reported for the preparation of crystallographically well-defined ceria nanocubes featuring enhanced photocatalytic response under visible light irradiation. The proposed approach relies on the *in situ* structural incorporation of 1,10-phenanthroline during crystal growth. Unlike conventional doping or surface functionalisation strategies, this method yields organic–inorganic nanostructured hybrid materials where the organic moiety is effectively incorporated into the fluorite-type ceria lattice through the formation of Ce–N coordination bonds while preserving the cubic morphology enclosed by reactive {100} facets and simultaneously increasing the specific surface area. Diffuse reflectance UV–Vis spectroscopy and valence band XPS analyses reveal that this integration induces the appearance of N $2p$ intraband gap states associated with the Ce–N bonds, resulting in a significant narrowing of the optical band gap and extending the light absorption edge into the visible region. Consequently, these organoceria hybrids exhibit a remarkable synergistic enhancement in photocatalytic hydrogen production *via* ethanol photoreforming under simulated solar irradiation, with hydrogen evolution rates being 7.5 times higher than those of pristine ceria nanocubes. This work demonstrates the potential of organic ligand-assisted lattice engineering as a versatile approach for tailoring the optoelectronic properties of ceria, thus opening new avenues for sustainable solar-to-chemical energy conversion.

[a]*Departamento de Ciencia de los Materiales e Ingeniería Metalúrgica y Química Inorgánica, Facultad de Ciencias, Universidad de Cádiz, Campus Río San Pedro s/n, 11510 Puerto Real, Cádiz, Spain*
[b]*Instituto Universitario de Investigación en Microscopía Electrónica y Materiales (IMEYMAT), Facultad de Ciencias, Universidad de Cádiz, Campus Río San Pedro s/n, 11510 Puerto Real, Cádiz, Spain*
[c]*Department of Chemical Engineering, University of the Basque Country UPV/EHU, P. O. Box 644, E48080 Bilbao, Spain*
[d]*School of Chemistry and Chemical Engineering, Queen's University Belfast, Belfast BT9 5AG, UK*
[e]*Departamento de Física de la Materia Condensada, Facultad de Ciencias, Universidad de Cádiz, Campus Río San Pedro s/n, 11510 Puerto Real, Cádiz, Spain*
[f]*GIR QUESCAT, Departamento de Química Inorgánica, Universidad de Salamanca, 37008 Salamanca, Spain. E-mail: adrianbogeat@usal.es*

Introduction

Since the mid-1970s, ceria (cerium dioxide, CeO_2) has become a ubiquitous material in the field of heterogeneous catalysis, being employed either as a catalyst or, much more frequently, as a non-inert support for catalysts and as a structural or electronic promoter.[1,2] Indeed, ceria is an essential material in the manufacture of modern three-way catalysts (TWCs), which is the most widespread and important catalytic application of this rare earth oxide in terms of establishment, economic relevance, and tonnage.[2]

In the last decade, a great deal of attention and growing research activity have been devoted to ceria and ceria-based materials as alternative photocatalysts to conventional titania (TiO_2), not only for wastewater treatment[3] but also for emerging processes, like water splitting for hydrogen generation[4] or carbon dioxide conversion into high added value products.[5] Similarly to titania, ceria is a wide band gap semiconductor oxide (E_g = 3.2–3.4 eV), so the photogeneration of charge carriers (*i.e.*, electron–hole pairs) requires absorption of ultraviolet (UV) light with wavelengths below 390 nm.[6] Accordingly, the rational design and synthesis of new ceria-based photocatalysts with improved absorption of visible light and accessible surfaces for target molecules are mandatory to make photocatalysis a sustainable technology, which enables the degradation of pollutants and production of chemicals using sunlight as a renewable energy source.[6] Currently, the challenge of boosting ceria photoactivity under visible light has been addressed by exploring the following main modification strategies: (i) metal and non-metal doping, (ii) design of hetero-

junctions by coupling with other semiconductor materials, and (iii) introduction of oxygen vacancies.[7] Among these methods, non-metal doping, and particularly nitrogen doping, has been profusely investigated. In addition to tuning the band gap of ceria from the UV to the visible region, the controlled incorporation of this element also enables the slow-down of the recombination rate of photogenerated electron–hole pairs and even improvement of the adsorption of acidic molecules, like CO_2.[7]

Herein, we report a novel synthetic strategy for the preparation of crystallographically well-defined ceria nanoparticles with a cubic morphology and featuring enhanced photocatalytic properties under visible light irradiation. Our strategy relies on the *in situ* incorporation of a classic, nitrogen-containing, heterocyclic organic ligand, namely 1,10-phenanthroline (phen, henceforth), during the hydrothermal synthesis of these ceria nanocubes under mild conditions. Beyond its well-known versatile chelating character,[8] which allows this molecule to form stable complexes with a variety of transition metal and lanthanoid cations, including Ce^{3+},[9–12] phen has been selected due to its exceptional electron transport and hole blocking properties,[13] both features being highly desirable for the development of more efficient photocatalytic systems. The resulting organoceria nanostructured hybrid materials thus benefit from a synergistic combination of the unique catalytic properties of ceria nanocubes, which predominantly expose {100} facets with enhanced reducibility,[14,15] and the boost in the optoelectronic properties arising from the incorporation of phen in the fluorite-type crystal structure.

Experimental

Materials and reagents

$Ce(NO_3)_3 \cdot 6H_2O$ (99.5%, Alfa Aesar), NaOH (99%, Scharlau), and 1,10-phenanthroline (phen, ≥99%, Sigma Aldrich) were used as received without any additional purification treatment. A homemade Teflon-lined stainless steel autoclave with a maximum volume of 250 mL was employed as a hydrothermal reactor.

Synthesis of organoceria nanostructured hybrid materials

Ceria–phen nanostructured hybrid materials were synthesised by slightly modifying a hydrothermal procedure previously reported in the literature[14] and later successfully applied by our research group.[16–18] This synthetic route allows for the controlled growth of ceria nanocrystals with a well-defined cubic morphology while ensuring the effective incorporation of the organic moiety into the oxide lattice.

In a typical synthesis process, the required amount of phen to achieve the target nominal phen/Ce molar ratio was first dissolved in 100 mL of an aqueous $Ce(NO_3)_3 \cdot 6H_2O$ solution (0.12 mol L^{-1}) under vigorous mechanical stirring at room temperature. The mixture was stirred for several hours until a progressive colour change from colourless to pale yellow was observed, indicating the formation of a complex between the

Ce^{3+} cations and the phen ligand in the aqueous phase.[18] Subsequently, this precursor solution was mixed with 140 mL of a concentrated NaOH aqueous solution (15.45 mol L^{-1}) in a polypropylene beaker, immediately leading to the formation of a greyish homogeneous suspension. After further stirring for 30 min, the suspension was transferred to a 250 mL Teflon-lined stainless steel autoclave. The sealed reactor was heated at 180 °C for 24 h in an electric oven and then allowed to cool down to room temperature. The resulting pale brown precipitate was recovered by centrifugation and thoroughly washed with deionised water until the supernatant reached neutral pH. The solid product was oven-dried at 80 °C overnight, gently ground in an agate mortar, and finally sieved to obtain a fine, homogeneous powder. The as-prepared organoceria nanostructured hybrids are hereafter denoted as "CeO_2 NCs_Phen-*Y.YY*", where *Y.YY* denotes the nominal phen/Ce molar ratio (*i.e.*, 0.04 and 0.08).

For comparison purposes, organic-free ceria nanoparticles with a well-defined cubic morphology were synthesised as a reference material by following the same hydrothermal procedure described above, but in the absence of the phen ligand. This control sample is henceforth referred to as "CeO_2 NCs".

Physicochemical characterisation

The integration of the phen moiety into the nanostructured ceria was investigated by X-ray photoelectron spectroscopy (XPS) and Fourier transform infrared (FT-IR) spectroscopy.

XPS analyses were carried out using a Kratos Axis Ultra[DLD] spectrometer, equipped with a monochromatised Al Kα X-ray source (1486.6 eV) operated at 150 W. High-resolution spectra were recorded in the Fixed Analyser Transmission (FAT) mode with a pass energy of 20 eV. The as-synthesised samples were mounted in their powdered form onto the sample holder using a conductive double-sided carbon tape. Surface charging effects were compensated by employing a Kratos coaxial charge neutraliser. The binding energy (BE) scale was calibrated using the C 1*s* signal of adventitious carbon, fixed at 284.8 eV in accordance with the literature.[19] Spectral processing, including peak deconvolution and quantification, was performed using CasaXPS software (version 2.3.26.PR1.0, Casa Software Ltd, Devon, UK).

FT-IR spectra were recorded in transmission mode using a PerkinElmer Spectrum Two spectrometer in the 4000–400 cm^{-1} range, averaging 10 scans at a resolution of 4 cm^{-1}. Samples were prepared as KBr pellets (sample/KBr mass ratio of 1/50) and compacted at 5 tonnes per cm^2 for 3 min. A pure KBr pellet of equivalent mass was used as a blank for background subtraction.

The amount of phen incorporated into organoceria hybrid materials was quantified by thermogravimetric analysis (TGA) using an SDT Q600 horizontal thermobalance (TA Instruments). Approximately 30 mg of each sample were heated from room temperature to 900 °C at a heating rate of 10 °C min^{-1} under a flow of pure oxygen (30 mL min^{-1} STP).

The crystalline structure of both the control and phen-doped nanomaterials was studied by powder X-ray diffraction

(PXRD). Patterns were recorded at room temperature using a Bruker D8 Advance diffractometer with Cu Kα radiation (λ = 0.154 nm). Data were acquired over a 2θ range of 10–90°, with a step size of 0.02° and an accumulation time of 38.4 s per step. The volume-weighted mean crystalline domain size (D) of the cubic fluorite-type ceria phase was estimated by applying the Scherrer equation to its most intense diffraction peak located at 28.5°. Instrumental line broadening was corrected using a quartz external standard.

The morphological and microstructural features were examined by scanning transmission electron microscopy (STEM) in an FEI Nova NanoSEM 450 microscope. The instrument was operated in a high vacuum mode at an accelerating voltage of 30 kV, providing a spatial resolution of 0.8 nm. For STEM analysis, small fractions of the as-prepared powdered samples were directly deposited onto holey carbon-coated copper grids without further treatment.

The specific surface area (S_{BET}) of the nanostructured ceria-based materials was assessed by applying the Brunauer–Emmett–Teller equation to their respective N_2 adsorption–desorption isotherms in the relative pressure range of 0.05–0.20. These isotherms were measured at −196 °C using a Quantachrome Autosorb iQ3 equipment. Prior to the measurements, approximately 100 mg of each sample was outgassed under vacuum at 200 °C for 2 h to ensure the removal of adsorbed moisture and atmospheric contaminants.

The optical band gaps (E_g) of the as-prepared pristine and phen-doped ceria nanostructured materials were estimated by diffuse reflectance ultraviolet-visible (DR-UV) spectroscopy. Spectra were recorded in air at room temperature in the 200–800 nm wavelength range using an Agilent Cary 5000 UV-Vis-NIR double-beam spectrophotometer, equipped with an integrating sphere. The experimental reflectance data were converted into the equivalent absorption coefficient by applying the Kubelka–Munk function, $F(R)$, according to the following expression:

$$F(R) = \frac{(1-R)^2}{2R} \qquad (1)$$

where R represents the diffuse reflectance of the sample as directly measured by the spectrophotometer. The E_g values were then estimated by the Tauc plot method.

Photocatalytic hydrogen production experiments

The photocatalytic hydrogen production experiments were carried out in a custom-designed on-line photoreactor, which allows simultaneously testing up to four different samples. A detailed description of this system can be found elsewhere.[20,21] A 450 W xenon lamp (Oriel Sol3A, Newport) was employed as the light source without any additional filter, and its stability was checked before and after each photocatalytic test. The irradiated area was 15.2 cm^2, while the sunlight irradiance was quantified to reach an intensity of 160 mW cm^{-2}. Furthermore, the reactor temperature was kept constant at 8 °C throughout the entire experiment.

In a standard photocatalytic test, 10 mg of either the undoped or phen-doped ceria nanomaterials were gently dispersed in 70 mL of a 50% (v/v) ethanol aqueous solution and then mechanically stirred at 800 rpm. Platinum was employed as a co-catalyst and photodeposited *in situ* by adding an appropriate volume of a $Pt(NO_3)_2$ aqueous solution prior to sealing the reactor, resulting in a final metal loading of 0.1 wt.%. After a leak test, the residual air in the reactor was purged by flowing argon at a rate of 15 mL min^{-1} for 2 h. This flow was kept constant during the photocatalytic runs and used as a carrier gas to analyse the reaction products using an online gas chromatograph (GC Trace 1300, Thermo Scientific) equipped with a thermal conductivity detector and a Carboxen 1010 PLOT capillary column.

Results and discussion

Synthesis and physicochemical characterisation of organoceria nanostructured hybrid materials

The successful incorporation of the phen ligand into the nanostructured hybrid materials was initially confirmed by the FT-IR spectroscopy technique. The spectra recorded for both the CeO$_2$ NCs_Phen-0.04 and CeO$_2$ NCs_Phen-0.08 samples are displayed in Fig. 1, along with those of pristine CeO$_2$ NCs and pure phen for comparison purposes.

The infrared spectrum of the undoped ceria nanomaterial is dominated by a sharp and very intense absorption peak at 1384 cm^{-1}. This characteristic signal, which is also clearly visible in the spectra of both organoceria samples, is ascribed to the asymmetric stretching mode (ν_3) of free nitrate (NO$_3^-$) ions,[22,23] originating from the cerium precursor salt and remaining in the solids even after thorough washing with deionised water. Additionally, a set of broad, low-intensity bands
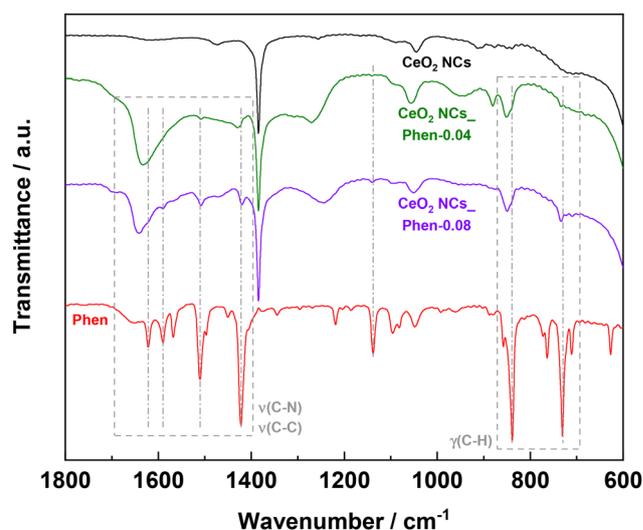

Fig. 1 FT-IR spectra of the CeO$_2$ NCs_Phen-0.04 and CeO$_2$ NCs_Phen-0.08 samples, as compared to those registered for the reference CeO$_2$ NCs material and pure phen.

appear in the 1800–1100 cm^{-1} region. These spectral features are attributed to a variety of surface carbonate and related species, formed through the interaction of ceria with atmospheric CO_2 during its preparation, handling, and storage.[24] Such species are ubiquitous on nanostructured ceria surfaces due to the well-established moderately basic character of this oxide.[25,26]

The spectroscopic analysis was essentially focused on the couple of frequency regions where the most prominent characteristic vibrations of the heterocyclic ligand typically appear, namely in the 1650–1400 cm^{-1} range, corresponding to the stretching vibration modes (ν) of the skeletal C–C and C–N aromatic bonds, and the 900–700 cm^{-1} region, associated with the out-of-plane bending vibration modes (γ) of C–H bonds on the heterocyclic rings and the centre ring.[27–30]

The FT-IR spectra of both phen-doped samples, particularly that of CeO_2 NCs_Phen-0.08, display the set of most intense absorption bands associated with the phen moiety, thus confirming the successful incorporation of the organic ligand into these nanomaterials. A detailed analysis reveals that the ν(C–C) and ν(C–N) peaks undergo a slight red shift toward lower wavenumbers relative to pure phen. In stark contrast, a blue shift is observed for the γ(C–H) vibrations. Such a bidirectional shift of the distinctive bands of the phen ligand is indicative of its effective coordination to the cerium cations within the ceria lattice. This interpretation is fully consistent with the frequency displacements registered for the same vibrational modes in the infrared spectrum of the $[Ce(NO_3)_3(phen)_2]$ complex,[18] and also aligns with reported trends for a wide range of metal-phen coordination compounds.[27,29,31–33] In addition, while the intensity of these characteristic absorption bands increases with the nominal phen loading, their positions remain invariant, thereby suggesting a consistent coordination environment across the phen-doped nanomaterials.

Finally, it is also worth mentioning that the marked increase in the intensity of the absorption bands is assigned to the surface carbonate and hydrogen carbonate species, such as those centred at around 1635 and 1270 cm^{-1}, as compared to the organic-free CeO_2 NCs. This observation is well in agreement with the expected increase in surface basicity upon incorporation of the phen dopant. The presence of this basic heterocyclic ligand likely promotes higher affinity for atmospheric CO_2, thereby resulting in a greater density of the adsorbed carbonate species on the surface of nanostructured ceria.

The above conclusions drawn from FT-IR spectroscopy regarding the effective incorporation of phen into the ceria lattice through coordination to cerium atoms were further supported by the XPS technique. The survey spectra of both organoceria samples confirm the presence of carbon and nitrogen, together with the constituent cerium and oxygen elements. A closer examination of the high-resolution core level spectra and the corresponding quantitative data reveals several key features related to the chemical environment and oxidation state of cerium, which are discussed below.

A primary observation concerns the oxidation state of cerium at the outermost surface layers, which undergoes rele-

vant changes upon doping. Strikingly, whereas the ligand-free CeO_2 NC reference exhibits a surface Ce^{3+} fraction of approximately 3%, the deconvolution of the Ce 3d core level signals (Fig. 2) indicates that surface cerium is exclusively present as Ce^{4+} in phen-doped nanomaterials. Consequently, the integration of phen into the ceria lattice leads to a marked depletion of Ce^{3+} species within the XPS probe depth, extending down to ca. 3.5 nm. This finding suggests the stabilisation of surface cerium in the +4 oxidation state induced by the presence of the nitrogen-containing heterocyclic ligand. Further insight into the oxidation state of cerium was obtained from the analysis of the valence band (VB) region (see Fig. 3). In this case, the appearance of a broad, low-intensity band located between 0.5 and 1.0 eV advocates for a Ce 4f population, which is characteristic of Ce^{3+} species.[34] Nevertheless, it is worth highlighting that this VB information originates from a depth of ca. 7 nm, nearly twice that provided by the Ce 3d core level signals. This observation could be indicative of the existence of a gradient in the cerium oxidation state, in which the Ce^{4+} stabilising effect of the phen molecule is markedly more pronounced at the outermost surface layers. In contrast, Ce^{3+} cations appear to persist in the deeper subsurface layers of the nanostructured ceria. Furthermore, the presence of these sub-
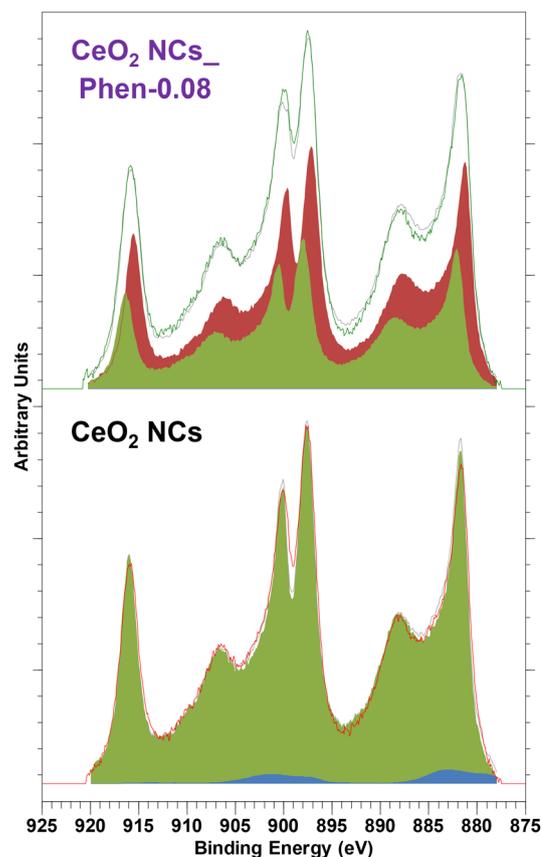

Fig. 2 High-resolution XPS spectra of the Ce 3d core level for the CeO_2 NCs_Phen-0.08 hybrid material, as compared to the phen-free CeO_2 NCs control sample.
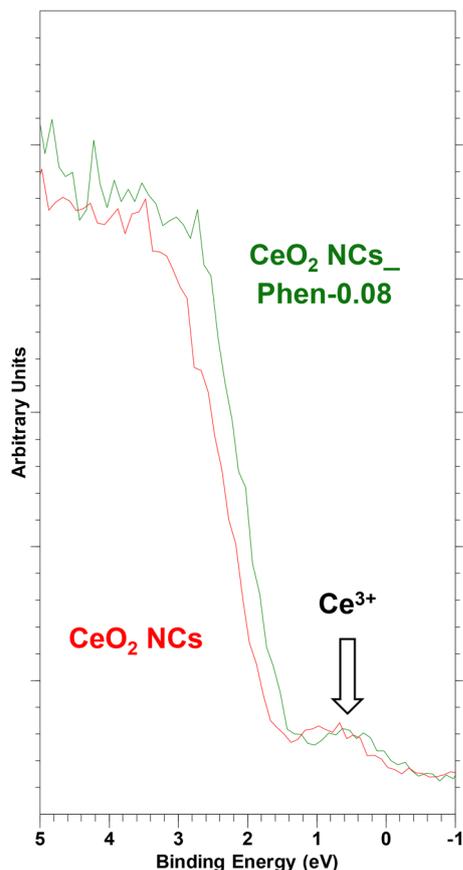
Fig. 3 High-resolution XPS spectra of the valence band region for the CeO$_2$ NCs_Phen-0.08 hybrid material, as compared to the phen-free CeO$_2$ NCs control sample.

surface Ce^{3+} species is inherently associated with the generation of oxygen vacancies to maintain charge neutrality in the fluorite lattice of ceria.

Secondly, the chemical environment of cerium cations in the organoceria hybrid materials was carefully analysed. The Ce 3d core level spectrum is highly complex due to multiplet splitting. Typically, it comprises three distinct peaks for each of the 3d$_{5/2}$ and 3d$_{3/2}$ components when both Ce^{3+} and Ce^{4+} species coexist in the material.[35–38] To ensure deconvolution reliability and minimise potential fitting errors associated with such a large number of required peaks, experimental high-resolution spectra for reference materials containing 100% Ce^{3+} and 100% Ce^{4+} were employed as standards.[39] Notably, while the Ce 3d profile of the control CeO$_2$ NCs was accurately fitted using the conventional multiplet peak structure, the spectra of the phen-containing nanomaterials exhibited significant deviations. Their most striking feature is the presence of unusually broad photoemission peaks, which point toward the coexistence of Ce^{4+} ions in two distinct chemical environments within the hybrid materials. Specifically, a major fraction of these cations, with the main component centred at *ca.* 882 eV, corresponds to a typical fluorite-type oxide environment. Conversely, some Ce^{4+} cations, which are coordinated to

the phen molecule, exhibit their most intense contribution at a slightly lower BE. This characteristic shift indicates an increased electron density in the vicinity of the cerium atoms as a result of their coordination with the nitrogen-donor ligand.[40] Importantly, since such unusual peak broadening is exclusively detected in the Ce 3d signals and is not observed for other core levels, any contribution arising from deficient surface charge compensation can be discarded.

A third significant aspect pertains to the N 1s core level region, which exhibits a clearly visible peak centred at approximately 398.7 eV, as shown in Fig. S1. This signal is shifted toward a lower BE with respect to pristine phen (399.5 eV)[41,42] and lies very close to the values reported for the N 1s peak in metal nitrides[40,43,44] and nitrogen-doped ceria.[45,46] Such a displacement provides clear evidence for the effective coordination of the nitrogen atoms to the cerium cations. Accordingly, it can be concluded that the Ce–N coordination bonds, initially established in aqueous solution during the first stage of the synthesis, are at least partially preserved in the resulting organoceria hybrids, despite the oxidation of cerium from the +3 to the +4 state occurring during the preparation process. Finally, as expected, the intensity of the N 1s signal increases with the nominal phen content in the doped nanomaterials.

Following the confirmation of phen incorporation into the ceria structure by spectroscopic techniques, the actual content of this organic ligand in both hybrid materials was quantified by thermogravimetric analysis (TGA) under a flow of pure oxygen. The recorded TG profiles, illustrated in Fig. 4 for the CeO$_2$ NCs_Phen-0.08 sample, exhibit a pronounced mass loss in the 300–400 °C temperature range, reaching its maximum rate at about 360 °C, as evidenced by the corresponding DTG curves. This thermal event is unambiguously assigned to the complete combustion of the coordinated phen moiety. Notably, the thermal decomposition of the ligand is markedly shifted to higher temperatures (by *ca.* 100 °C) compared to the pristine organic compound.[30,47] Such a remarkable enhance-
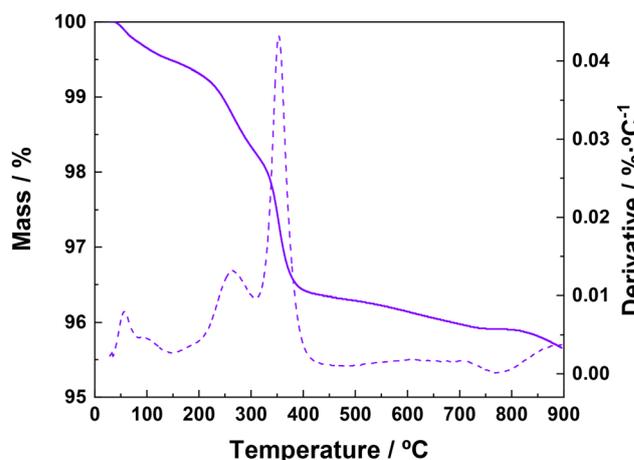

Fig. 4 TG and DTG profiles recorded under flowing oxygen (30 cm^3 mL^{-1}) for the CeO$_2$ NCs_Phen-0.08 hybrid material.

ment in thermal stability further supports the effective incorporation of the ligand into the ceria structure through coordination of its nitrogen atoms to the cerium centres.

The total phen content in the organoceria hybrids, as estimated from the mass loss in their TG curves, is significantly lower than the corresponding nominal values (Table 1). Specifically, the incorporation provides *ca.* 20% yields, irrespective of the initial phen/Ce molar ratio. This finding indicates that an important fraction of the organic compound either remained in solution or underwent partial degradation under hydrothermal synthesis conditions. Nevertheless, these relatively low phen loadings incorporated into the organoceria samples induce a remarkable impact on the optoelectronic properties, most notably the band gap, of the pristine nanostructured ceria, as will be discussed in detail later.

Once the effective incorporation of phen into the ceria lattice had been confirmed and quantified, the structure of the as-prepared organoceria samples was examined at a macroscopic scale using the PXRD technique. The diffractograms acquired for these hybrids are shown in Fig. 5, together with that of the control undoped CeO_2 NCs and a reference pattern of cubic fluorite ceria (space group $Fm\bar{3}m$, JCPDS card no. 34-0394) for comparison. From this figure, it becomes evident that all experimental diffractograms are dominated by a series of sharp and well-defined reflections, which can be indexed to CeO_2 with a cubic fluorite-type structure. Notably, the absence of additional diffraction peaks excludes the formation of secondary cerium-containing crystalline phases upon phen incorporation, thereby confirming the monophasic nature of the doped nanomaterials. The only noticeable difference among these patterns is a slight broadening of the reflection peaks for the organoceria samples (see Fig. S2), indicative of a reduction in their average crystalline domain size (D). In this regard, estimates obtained from the Scherrer equation applied to the (111) reflection at $2\theta = 28.5°$ (Table 1) reveal that the crystalline domain size decreases from approximately 45 nm in the phen-free reference material to about 25 nm for the CeO_2 NCs_Phen-0.08 sample. Accordingly, the incorporation of phen induces a certain kinetic hindrance to the crystallisation of the ceria phase during hydrothermal treatment. This effect is most likely associated with the coordination of the nitrogen-containing heterocyclic ligand to cerium atoms within the oxide lattice, thus stabilising smaller crystalline nuclei and limiting their subsequent growth. Finally, the lattice spacing

(d) of *ca.* 0.31 nm estimated for both organoceria hybrids from their PXRD patterns is fully consistent with the interplanar distance of the (111) planes of cubic fluorite-type ceria.

With regard to the morphological features of the as-synthesised ceria nanomaterials, representative STEM images displayed in Fig. 6 clearly demonstrate that these samples consist of nanocrystalline particles with a well-defined cubic shape, predominantly bounded by {100} facets. The edge lengths of these nanocubes span a relatively broad range, from around 5 to 80 nm. Notably, the average particle size (see Table 1) is smaller for the organoceria hybrid materials compared to the control ceria sample, in good agreement with the decrease in the mean crystalline domain size previously derived from PXRD analysis. Such a decrease in particle size is accompanied by a noticeable increase in their specific surface area (S_{BET}), which rises from 20.5 $m^2 \cdot g^{-1}$ for the pristine organic-free reference to values close to 30 $m^2 \cdot g^{-1}$ for phen-containing nanostructured materials. Taken together, these experimental results suggest that phen behaves as a size-regulating agent during hydrothermal synthesis. By coordinating to cerium atoms, the ligand partially slows down the crystallisation rate and limits the growth of the ceria phase while preserving its characteristic cubic morphology.

The potential applicability of the as-synthesised organoceria hybrids in photocatalytic processes critically depends on their activation under visible light. Among the various strategies commonly explored to achieve this goal, band gap engineering through the selective introduction of intermediate electronic states is considered a particularly effective approach, as it enables the precise modulation of the relative positions of the conduction and valence band edges. In this work, the optical band gap was estimated by applying the Kubelka–Munk function to the DR-UV spectra, while the maximum energy of the VB was determined by analysing the VB region of the XPS spectra (see the Experimental section for further details).

Data summarised in Table 1 and the DR-UV spectra shown in Fig. 7 confirm that the incorporation of the phen moiety during the synthesis of the ceria nanocubes induces narrowing of the optical band gap, from 3.23 eV for the organic-free control CeO_2 NCs to 3.11 eV for the CeO_2 NCs_Phen-0.08 hybrid. This red shift effect is primarily attributed to the appearance of intermediate N 2p energy levels associated with the Ce–N coordination bonds, which are maintained through-

Table 1 Nominal and actual phen contents, structural parameters, specific surface areas, and optical band gap values of the organoceria nanostructured hybrid materials and the phen-free CeO_2 NCs control sample

Sample	Nominal phen content/wt.%	phen[a]/wt.%	D^b/nm	D^c/nm	$d_{(111)}{}^d$/nm	$S_{BET}{}^e$/$m^2\ g^{-1}$	$E_g{}^f$/eV
CeO_2 NCs	—	—	46.5	47.0	0.31	20.5	3.23
CeO_2 NCs_Phen-0.04	4.2	0.9	38.7	40.3	0.31	27.8	3.17
CeO_2 NCs_Phen-0.08	8.0	1.8	25.5	27.3	0.31	29.5	3.11

[a] Actual phen content from TG analyses. [b] Average crystalline domain size as estimated from PXRD. [c] Mean particle size as determined from STEM. [d] Ceria lattice spacing from PXRD. [e] Specific surface area from N_2 adsorption/desorption isotherms. [f] Band gap energy as calculated from the Tauc plot.
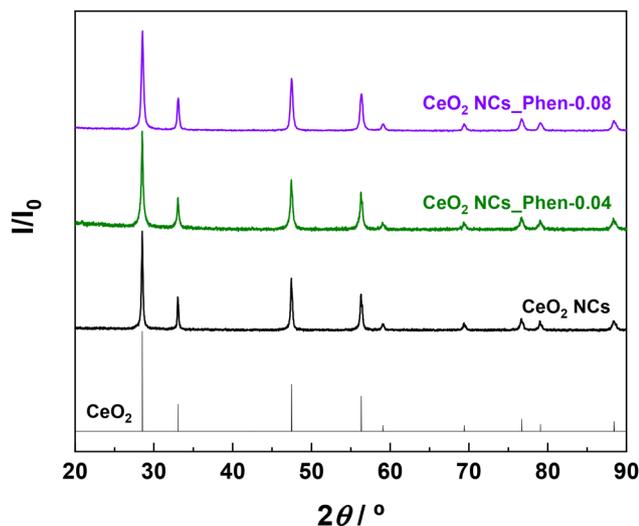
Fig. 5 PXRD patterns of the as-prepared organoceria hybrid materials compared to the phen-free CeO$_2$ NCs control sample.

Fig. 7 DR-UV spectra recorded for the as-prepared organoceria hybrid materials and the phen-free CeO$_2$ NCs control sample.

out the hydrothermal synthesis of the nanostructured hybrid materials, as evidenced by XPS analysis. Such intraband gap states are expected to act as "stepping stones" for electronic transitions, thereby enabling the photoactivation of the organoceria samples under visible light irradiation. In line with this interpretation, the appearance of additional distinct absorption edges at wavelengths beyond 400 nm in the DR-UV spectra of the phen-doped samples (Fig. 7) provides further evidence for the formation of the aforesaid intermediate electronic levels.[48,49] Consequently, it can be concluded that long wavelength visible light is capable of promoting electron–hole pair generation in the as-prepared organoceria hybrids,[50] thus contributing to extending their photoresponse into the visible region. Finally, a shift of *ca.* 0.16 eV to a lower BE in the VB maximum energy is observed for the CeO$_2$ NCs_Phen-0.08 hybrid relative to the undoped control CeO$_2$ NCs (see Fig. 3). This finding is also well in agreement with the modification of the electronic structure due to the presence of inter-
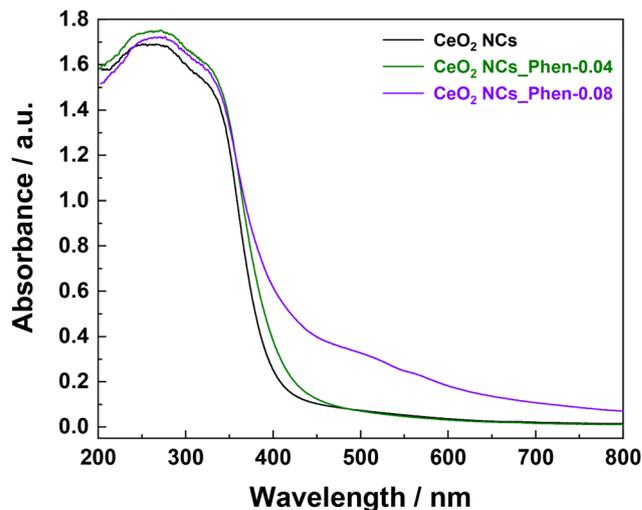
mediate N 2p energy levels arising from the incorporation of the phen ligand.

Photocatalytic activity

The photocatalytic performance of the as-synthesised organoceria hybrid materials was explored in the ethanol photoreforming hydrogen production under simulated solar irradiation, employing a low platinum co-catalyst loading (0.05 wt.%). In contrast to methanol, which is the most widely investigated sacrificial agent but is predominantly derived from fossil fuels (syngas), ethanol was selected as a model compound due to its renewable origin. Indeed, ethanol can be obtained from biomass by the fermentation of lignocellulosic-derived sugars[51] or directly from CO$_2$ using genetically engineered microorganisms.[52] Consequently, ethanol can be regarded as a carbon-neutral and sustainable feedstock for photocatalytic hydrogen production.

The results of these photocatalytic experiments for both the organoceria samples and the phen-free control are displayed in Fig. 8 as cumulative hydrogen yield *vs.* irradiation time plots. The photocatalytic hydrogen production rates, as estimated from linear fitting of the experimental data, are comparable for the undoped reference material (19.5 μmol (g h)$^{-1}$) and the CeO$_2$ NCs_Phen-0.04 hybrid (20.3 μmol (g h)$^{-1}$). In stark contrast, the CeO$_2$ NCs_Phen-0.08 sample exhibits an outstanding enhancement in photocatalytic performance, with a hydrogen evolution rate of 153.0 μmol (g h)$^{-1}$, which represents an approximately 7.5-fold increase in activity relative to both the pristine CeO$_2$ NCs and the lower phen-loading counterpart. Overall, these results clearly reveal that the incorporation of the phen moiety through the proposed novel synthetic approach leads to a marked improvement in the photocatalytic activity of nanostructured ceria, provided that a doping threshold is reached. Furthermore, it is also worth highlighting that no significant deactivation was detected
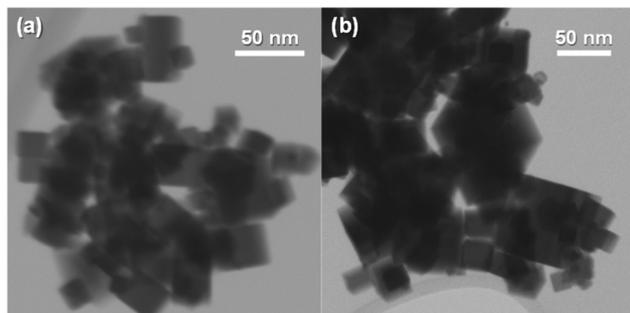

Fig. 6 Representative STEM images of (a) the CeO$_2$ NCs_Phen-0.08 hybrid material and (b) the organic-free CeO$_2$ NCs reference sample.
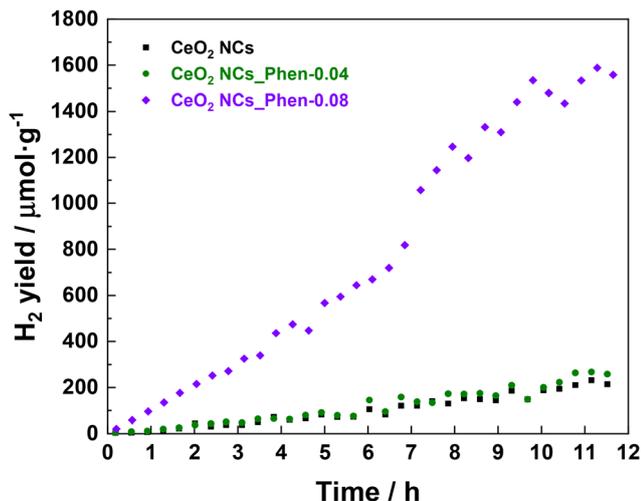
Fig. 8 Photocatalytic hydrogen production yield as a function of irradiation time for the as-prepared organoceria hybrid materials and the phen-free CeO$_2$ NCs control sample.

achieved using a significantly lower photocatalyst mass compared to most reported studies.

The outstanding performance of the CeO$_2$ NCs_Phen-0.08 hybrid in the ethanol photoreforming hydrogen production, as compared to the pristine organic-free reference, is primarily attributed to a synergistic combination of a significant narrowing of the optical band gap and the appearance of additional absorption edges at wavelengths above 400 nm. Both effects are likely associated with the presence of N 2p intraband gap states, which arises from the formation of Ce–N coordination bonds.[30] These intraband states not only extend the light-harvesting capability of nanostructured ceria into the visible region but also act as intermediate steps for charge carrier excitation. Finally, it should be noted that the observed enhancement in photocatalytic performance cannot be correlated with an increased surface density of Ce^{3+} species or its associated oxygen vacancies, which are typically considered in the literature as responsible for improved activity in ceria-based photocatalysts.[53]

during the photocatalytic tests for both the organocerias and the control sample, as evidenced by the relatively stable hydrogen production rates maintained over a continuous irradiation period of 12 h. Such stability strongly suggests that the phen molecules are effectively integrated into the ceria lattice, thus preventing ligand leaching or photodegradation under the operating conditions of ethanol photoreforming.

Establishing a direct comparison with previously reported data is challenging due to the diverse experimental conditions employed in the literature. Nonetheless, Table 2 summarises the photocatalytic hydrogen production performance for several representative ceria-based materials, both in the presence and absence of co-catalysts. Notably, the hydrogen evolution yield of the CeO$_2$ NCs_Phen-0.08 hybrid markedly surpasses the values reported for many ceria photocatalytic systems. In this regard, it is also noteworthy that the high photocatalytic activity reported in the present work was

Table 2 Comparison of the photocatalytic hydrogen production performance of representative ceria-based materials with and without co-catalysts

Sample mass/mg	Co-catalyst	Reducing agent	Power of the light source/W	λ/nm	H$_2$ yield/ μmol (g h)$^{-1}$	Ref.
10	Pt	Ethanol	450	>200	153.0	This work
30	—	Methanol	—	>400	68	54
50	—	—	400	>200	12.5	55
1000	—	—	450	>200	7.1	56
1000	Pt	—	450	>200	7.7	56
1000	Li	—	450	>200	8.4	56
1000	Cs	—	450	>200	81.6	56
100	—	Na$_2$S + Na$_2$SO$_3$	300	>200	5.0	57
10	—	Ethanol	225	>200	112	58

Conclusions

In this work, a novel synthetic strategy has been developed for the preparation of crystallographically well-defined ceria nanocubes with enhanced photocatalytic performance under visible light irradiation. The proposed approach relies on the *in situ* incorporation of phen, a typical nitrogen-containing heterocyclic ligand, during a conventional hydrothermal synthesis under mild conditions. This methodology allows for the effective integration of the organic moiety into the fluorite-type ceria lattice while preserving the cubic morphology enclosed by the highly reactive {100} facets and simultaneously modulating the electronic structure of the oxide.

The as-synthesised organoceria nanostructured hybrid materials exhibit improved visible light harvesting, which is primarily attributed to the formation of Ce–N coordination bonds. These interactions lead to the appearance of N 2p intraband gap states, which effectively narrow the optical band gap and provide intermediate levels for visible light-driven charge carrier excitation. Such electronic structure modification translates into an outstanding photocatalytic performance for hydrogen production *via* ethanol photoreforming under simulated solar irradiation. Notably, the CeO$_2$ NCs_Phen-0.08 hybrid achieves a hydrogen production rate approximately 7.5 times higher than that of the pristine ceria nanocubes. Furthermore, the organoceria hybrids exhibit good operational stability, with no significant deactivation observed over a prolonged irradiation time of 12 h, a period that significantly exceeds the typical testing times reported for ceria-based photocatalysts in the literature (often ranging from 30 min to 6 h). This stability indicates a strong integration of phen within the oxide lattice and resistance to leaching or photodegradation under reaction conditions.

Overall, this study reveals that the incorporation of an appropriate organic ligand during crystal growth constitutes

an effective and versatile approach for engineering the electronic structure of ceria nanostructures and extending their photoresponse into the visible region. The proposed approach paves the way for the rational design of organic–inorganic hybrid photocatalysts based on ceria with tailored optoelectronic properties for sustainable hydrogen production and other solar-to-fuel conversion processes.

Author contributions

Conceptualization: GB and ABB; formal analysis: EB, DG, AA, GB, and ABB; funding acquisition: JJD and GB; investigation: MPJ, EB, DG, AA, GB, and ABB; methodology: JJD, JMP, GB, and ABB; resources: DG, JJD, and JMP; supervision: GB and ABB; validation: DG, GB, and ABB; visualization: EB, DG, AA, GB, and ABB; writing – original draft: ABB; and writing – review & editing: DG, JMP, GB, and ABB.

Conflicts of interest

There are no conflicts to declare.

Data availability

The datasets generated during this study are fully available within the article and its supplementary information (SI). Supplementary information is available. See DOI: https://doi.org/10.1039/d6dt00140h.

Acknowledgements

References

1 A. Trovarelli and P. Fornasiero, *Catalysis by ceria and related materials*, Imperial College Press, London, 2nd edn, 2013.

2 T. Montini, M. Melchionna, M. Monai and P. Fornasiero, *Chem. Rev.*, 2016, **116**, 5987–6041.

3 P. Ji, J. Zhang, F. Chen and M. Anpo, *Appl. Catal., B*, 2009, **85**, 148–154.

4 A. Primo, T. Marino, A. Corma, R. Molinari and H. García, *J. Am. Chem. Soc.*, 2011, **133**, 6930–6933.

5 D. Jiang, W. Wang, E. Gao, S. Sun and L. Zhang, *Chem. Commun.*, 2014, **50**, 2005–2007.

6 S. Xie, Z. Wang, F. Cheng, P. Zhang, W. Mai and Y. Tong, *Nano Energy*, 2017, **34**, 313–337.

7 D. P. H. Tran, M.-T. Pham, X.-T. Bui, Y.-F. Wang and S.-J. You, *Sol. Energy*, 2022, **240**, 443–466.

8 A. Bencini and V. Lippolis, *Coord. Chem. Rev.*, 2010, **254**, 2096–2180.

9 F. A. Hart and F. P. Laming, *J. Inorg. Nucl. Chem.*, 1964, **26**, 579–585.

10 Q.-Y. Lin and Y.-L. Feng, *Z. Kristallogr. - New Cryst. Struct.*, 2003, **218**, 531–532.

11 Nibha, B. P. Baranwal, G. Singh and C. G. Daniliuc, *J. Rare Earths*, 2014, **32**, 545–552.

12 A. V. Shurygin, V. I. Vovna, V. V. Korochentsev, A. G. Mirochnik, I. V. Kalinovskaya and V. I. Sergienko, *Spectrochim. Acta, Part A*, 2019, **213**, 176–183.

13 C. Sun, Y. Wu, W. Zhang, N. Jiang, T. Jiu and J. Fang, *ACS Appl. Mater. Interfaces*, 2014, **6**, 739–744.

14 H.-X. Mai, L.-D. Sun, Y.-W. Zhang, R. Si, W. Feng, H.-P. Zhang, H.-C. Liu and C.-H. Yan, *J. Phys. Chem. B*, 2005, **109**, 24380–24385.

15 T. Désaunay, G. Bonura, V. Chiodo, S. Freni, J.-P. Couzinié, J. Bourgon, A. Ringuedé, F. Labat, C. Adamo and M. Cassir, *J. Catal.*, 2013, **297**, 193–201.

16 A. Barroso-Bogeat, G. Blanco, J. J. Pérez-Sagasti, C. Escudero, E. Pellegrin, F. C. Herrera and J. M. Pintado, *Materials*, 2021, **14**, 711.

17 A. Barroso Bogeat, G. Blanco, J. M. Pintado, D. Goma and J. J. Calvino Gámez, *Surf. Interfaces*, 2021, **26**, 101353.

18 M. Puerto-Jiménez, D. Goma, A. Aguinaco, E. López-Maya, M. G. Álvarez, J. M. Pintado, G. Blanco and A. Bogeat-Barroso, *Inorg. Chem. Commun.*, 2024, **164**, 112399.

19 T. L. Barr and S. Seal, *J. Vac. Sci. Technol., A*, 1995, **13**, 1239–1246.

20 E. Bu, X. Chen, C. López-Cartes, F. Cazaña, A. Monzón, J. Martínez-López and J. J. Delgado, *Catal. Today*, 2023, **422**, 114220.

21 E. Bu, X. Chen, C. López-Cartes, A. Monzón and J. J. Delgado, *J. Colloid Interface Sci.*, 2024, **676**, 1055–1067.

22 M. Y. Mihaylov, V. R. Zdravkova, E. Z. Ivanova, H. A. Aleksandrov, P. St. Petkov, G. N. Vayssilov and K. I. Hadjiivanov, *J. Catal.*, 2021, **394**, 245–258.

23 A. Bogeat-Barroso, M. F. Alexandre-Franco, C. Fernández-González and V. G. Serrano, *Compounds*, 2025, **5**, 36.

24 G. Finos, S. Collins, G. Blanco, E. Del Rio, J. M. Cíes, S. Bernal and A. Bonivardi, *Catal. Today*, 2012, **180**, 9–18.

25 S. Bernal, G. Blanco, J. J. Calvino, J. A. Pérez Omil and J. M. Pintado, *J. Alloys Compd.*, 2006, **408–412**, 496–502.

26 S. Sato, R. Takahashi, M. Kobune and H. Gotoh, *Appl. Catal., A*, 2009, **356**, 57–63.

27 A. A. Schilt and R. C. Taylor, *J. Inorg. Nucl. Chem.*, 1959, **9**, 211–221.

28 S. S. Singh, *Z. Naturforsch., A:Phys. Sci.*, 1969, **24**, 2015–2016.

29 T. P. Gerasimova and S. A. Katsyuba, *Dalton Trans.*, 2013, **42**, 1787–1797.

30 G. Sarigul, I. Gómez-Palos, N. Linares, J. García-Martínez, R. D. Costa and E. Serrano, *J. Mater. Chem. C*, 2020, **8**, 12495–12508.

31 M. M. Campos-Vallette, R. E. Clavijo, F. Mendizabal, W. Zamudio, R. Baraona and G. Diaz, *Vib. Spectrosc.*, 1996, **12**, 37–44.

32 V. Amani, N. Safari, H. R. Khavasi and P. Mirzaei, *Polyhedron*, 2007, **26**, 4908–4914.

33 D. J. Awad, F. Conrad, A. Koch, U. Schilde, A. Pöppl and P. Strauch, *Inorg. Chim. Acta*, 2010, **363**, 1488–1494.

34 L. Cardenas, C. Molinet-Chinaglia and S. Loridant, *Phys. Chem. Chem. Phys.*, 2022, **24**, 22815–22822.

35 P. Burroughs, A. Hamnett, A. F. Orchard and G. Thornton, *J. Chem. Soc., Dalton Trans.*, 1976, **33**, 1686–1698.

36 M. Romeo, K. Bak, J. El Fallah, F. Le Normand and L. Hilaire, *Surf. Interface Anal.*, 1993, **20**, 508–512.

37 E. Paparazzo, G. M. Ingo and N. Zacchetti, *J. Vac. Sci. Technol., A*, 1991, **9**, 1416–1420.

38 A. Kotani and H. Ogasawara, *J. Electron Spectrosc. Relat. Phenom.*, 1997, **86**, 65–72.

39 S. Fernandez-Garcia, L. Jiang, M. Tinoco, A. B. Hungria, J. Han, G. Blanco, J. J. Calvino and X. Chen, *J. Phys. Chem. C*, 2016, **120**, 1891–1901.

40 N. V. Somov, F. F. Chausov, I. S. Kazantseva, V. L. Vorob'yov, M. Anatol'evna Shumilova and A. N. Maratkanova, *J. Mol. Struct.*, 2022, **1270**, 133935.

41 C. Ferragina, M. A. Massucci and G. Mattogno, *J. Inclusion Phenom.*, 1989, **7**, 529–536.

42 J. Casanovas, J. M. Ricart, J. Rubio, F. Illas and J. M. Jiménez-Mateos, *J. Am. Chem. Soc.*, 1996, **118**, 8071–8076.

43 B. M. Biwer and S. L. Bernasek, *J. Electron Spectrosc. Relat. Phenom.*, 1986, **40**, 339–351.

44 T. B. Thiede, M. Krasnopolski, A. P. Milanov, T. de los Arcos, A. Ney, H.-W. Becker, D. Rogalla, J. Winter, A. Devi and R. A. Fischer, *Chem. Mater.*, 2011, **23**, 1430–1440.

45 A. B. Jorge, J. Fraxedas, A. Cantarero, A. J. Williams, J. Rodgers, J. P. Attfield and A. Fuertes, *Chem. Mater.*, 2008, **20**, 1682–1684.

46 C. Mao, Y. Zhao, X. Qiu, J. Zhu and C. Burda, *Phys. Chem. Chem. Phys.*, 2008, **10**, 5633–5638.

47 Z. A. Taha, A. M. Ajlouni, T. S. Ababneh, W. Al-Momani, A. K. Hijazi, M. Al Masri and H. Hammad, *Struct. Chem.*, 2017, **28**, 1907–1918.

48 P. Makuła, M. Pacia and W. Macyk, *J. Phys. Chem. Lett.*, 2018, **9**, 6814–6817.

49 G. Sarigul, I. Chamorro-Mena, N. Linares, J. García-Martínez and E. Serrano, *Adv. Sustainable Syst.*, 2021, **5**, 2100076.

50 S. Kalathil, M. M. Khan, S. A. Ansari, J. Lee and M. H. Cho, *Nanoscale*, 2013, **5**, 6323–6326.

51 B. Hahn-Hägerdal, M. Galbe, M. F. Gorwa-Grauslund, G. Lidén and G. Zacchi, *Trends Biotechnol.*, 2006, **24**, 549–556.

52 Z. Gao, H. Zhao, Z. Li, X. Tan and X. Lu, *Energy Environ. Sci.*, 2012, **5**, 9857–9865.

53 A. S. Thill, F. O. Lobato, M. O. Vaz, W. P. Fernandes, V. E. Carvalho, E. A. Soares, F. Poletto, S. R. Teixeira and F. Bernardi, *Appl. Surf. Sci.*, 2020, **528**, 146860.

54 Y. Huang, C.-F. Yan, C.-Q. Guo and Y. Shi, *Int. J. Hydrogen Energy*, 2016, **41**, 7919–7926.

55 J. Krishna Reddy, G. Suresh, C. H. Hymavathi, V. Durga Kumari and M. Subrahmanyam, *Catal. Today*, 2009, **141**, 89–93.

56 K.-H. Chug and D.-C. Park, *Catal. Today*, 1996, **30**, 157–162.

57 B. Dong, L. Li, Z. Dong, R. Xu and Y. Wu, *Int. J. Hydrogen Energy*, 2018, **43**, 5275–5282.

58 A. S. Thill, F. O. Lobato, M. O. Vaz, W. P. Fernandes, V. E. Carvalho, E. A. Soares, F. Poletto, S. R. Teixeira and F. Bernardi, *Appl. Surf. Sci.*, 2020, **528**, 146860.